Chemical Science

ROYAL SOCIETY OF CHEMISTRY

EDGE ARTICLE

View Article Online
View Journal | View Issue

Cite this: *Chem. Sci.*, 2024, **15**, 3957

All publication charges for this article have been paid for by the Royal Society of Chemistry

Received 13th October 2023
Accepted 23rd January 2024

DOI: 10.1039/d3sc05450k

rsc.li/chemical-science

Switching the proton-coupled electron transfer mechanism for non-canonical tyrosine residues in a *de novo* protein†

Astrid Nilsen-Moe,[a] Clorice R. Reinhardt,[b] Ping Huang,[a] Hemlata Agarwala,[c] Rosana Lopes,[d] Mauricio Lasagna,[d] Starla Glover,[a] Sharon Hammes-Schiffer,[e] Cecilia Tommos *[d] and Leif Hammarström *[a]

The proton-coupled electron transfer (PCET) reactions of tyrosine (Y) are instrumental to many redox reactions in nature. This study investigates how the local environment and the thermodynamic properties of Y influence its PCET characteristics. Herein, 2- and 4-mercaptophenol (MP) are placed in the well-folded α_3C protein (forming 2MP-α_3C and 4MP-α_3C) and oxidized by external light-generated $[Ru(L)_3]^{3+}$ complexes. The resulting neutral radicals are long-lived (>100 s) with distinct optical and EPR spectra. Calculated spin-density distributions are similar to canonical Y$^{\bullet}$ and display very little spin on the S–S bridge that ligates the MPs to C_{32} inside the protein. With 2MP-α_3C and 4MP-α_3C we probe how proton transfer (PT) affects the PCET rate constants and mechanisms by varying the degree of solvent exposure or the potential to form an internal hydrogen bond. Solution NMR ensemble structures confirmed our intended design by displaying a major difference in the phenol OH solvent accessible surface area ($\leq\sim$2% for 2MP and 30–40% for 4MP). Additionally, 2MP-C_{32} is within hydrogen bonding distance to a nearby glutamate (average O–O distance is 3.2 $\pm$ 0.5 Å), which is suggested also by quantum mechanical/molecular mechanical (QM/MM) molecular dynamics simulations. Neither increased exposure of the phenol OH to solvent (buffered water), nor the internal hydrogen bond, was found to significantly affect the PCET rates. However, the lower phenol pK_a values associated with the MP-α_3C proteins compared to α_3Y provided a sufficient change in PT driving force to alter the PCET mechanism. The PCET mechanism for 2MP-α_3C and 4MP-α_3C with moderately strong oxidants was predominantly step-wise PTET for pH values, but changed to concerted PCET at neutral pH values and below when a stronger oxidant was used, as found previously for α_3Y. This shows how the balance of ET and PT driving forces is critical for controlling PCET mechanisms. The presented results improve our general understanding of amino-acid based PCET in enzymes.

Introduction

Proton-coupled electron transfer (PCET) is a fundamental process that is ubiquitous in natural and synthetic redox chemistry and catalysis. Understanding how PCET functions in biochemical systems unlocks the potential to take advantage of the same basic principles in synthetic designs. PCET can proceed *via* a step-wise mechanism where electron transfer (ET) and proton transfer (PT) advance one after the other (PTET or ETPT), or *via* a concerted mechanism (CEPT) where both ET and PT proceed in one kinetic step. Theoretical and small-molecule experimental studies have shown that PCET rate constants and mechanisms depend on the driving forces for electron and proton transfer, ΔG°_{ET} and ΔG°_{PT}, electron and proton transfer (tunneling) distances, and the reorganization energy, λ.[1–4] Systematic studies that examine how PCET is affected by changing ΔG°_{ET} and ΔG°_{PT} are important to advance our understanding of PCET in biology and chemistry.

Some oxidoreductases use tyrosine (Y), tryptophan (W), glycine, and/or cysteine residues as $1e^-$ redox (radical) cofactors.[3,5] Amino-acid oxidation–reduction typically involves PCET, with the exception of W which participates in both $1e^-$ and $1e^-/1H^+$ reactions. In the context of PCET, ΔG°_{PT} is determined by the pK_a of the amino acid and the pK_a of the primary proton acceptor. The latter may be a protein residue, a cofactor, buffer

[a]*Department of Chemistry, Ångström Laboratory, Uppsala University, Box 523, 75120 Uppsala, Sweden. E-mail: leif.hammarstrom@kemi.uu.se*

[b]*Department of Molecular Biophysics and Biochemistry, Yale University, New Haven, CT 06520, USA*

[c]*Technical University Munich, Campus Straubing for Biotechnology and Sustainability, Uferstraße 53, 94315 Straubing, Germany*

[d]*Department of Biochemistry and Biophysics, Texas A&M University, College Station, TX 77843, USA. E-mail: tommos@tamu.edu*

[e]*Department of Chemistry, Yale University, New Haven, CT 06520, USA*

† Electronic supplementary information (ESI) available. See DOI: https://doi.org/10.1039/d3sc05450k

and/or water species. Modulating the ΔG°_{ET} and/or ΔG°_{PT} parameter(s) can change the mechanism between step-wise and concerted PCET.[1] This has important consequences for the rate of radical generation and transfer. If PCET is a part of the rate-limiting step in a catalytic cycle, changes in the mechanism can consequently affect catalytic behavior and performance.

Here we use the α_3X protein model system to alter the local environment of a Y redox site and investigate if, and in that case how, the structural changes alter the PCET properties. The α_3X family of well-structured model proteins is based on a 65-residue, pH stable and redox inert three-helix bundle (α_3).[5,6] The α_3 scaffold hosts a single redox-active Y or W residue at interior position 32 (X_{32}). Oxidation-reduction of X_{32} is reversible, allowing accurate midpoint potentials, $E^{o\prime}$, (*i.e.*, [radical]/[reduced species] = 1) to be obtained.[7,8] This represents a major advantage of using the α_3X model system to characterize amino-acid based PCET reactions. Additionally, the broad pH stability of the α_3X proteins allows PCET characterization as a function of pH. Tommos *et al.* introduced a series of non-canonical Y residues at site 32, including aminotyrosine (α_3(NH_2)Y), fluorotyrosines (α_3(F_n)Y, n = 2, 3), and covalently bound mercaptophenols (2MP- and 4MP-α_3C).[8–11] With these Y analogs, the $E^{o\prime}$($X_{32}^{\bullet}$/X_{32}) and the phenol pK_a could be expanded across a range of 722 mV and 4.1 pK_a units, respectively.[5] In this study, we report the structural, spectroscopic, and radical ($X_{32}^{\bullet}$) formation and decay characteristics of 2MP-α_3C and 4MP-α_3C relative to those of α_3Y. Previous studies using external $[Ru(bpy)_3]^{3+}$ (bpy = 2,2′-bipyridine) oxidants showed that the $1e^-/1H^+$ oxidation of Y_{32} is pH-dependent with CEPT dominating at low pH and pre-equilibrium PTET dominating at high pH.[12,13] Water (H_2O) was assigned as the dominant primary proton acceptor for the CEPT mechanism. $Y_{32}^{\bullet}$ was shown to be long-lived ($t_{1/2}$ = 2–10 s) and to decay *via* radical–radical dimerization.[12]

The MP-α_3C proteins were designed to specifically modulate interactions at the phenol OH group. By ligating the different MPs to the buried C_{32} residue, the aim was to shift the phenol OH from the protein interior (2MP-α_3C, Fig. 1A) towards the protein surface (4MP-α_3C, Fig. 1C).[9] The solution nuclear magnetic resonance (NMR) structure of 2MP-α_3C confirmed the intended design for this protein.[14] This structure also revealed that 2MP-C_{32} is involved in a weak, interhelical hydrogen bond (H-bond) with the sidechain oxygen(s) of E_{13}. The solution NMR structure of 4MP-α_3C, presented herein, solidifies the protein design further by showing that the solvent accessible surface area (SASA) of the phenol OH changes from ≤∼2% in 2MP-α_3C to 30–40% in 4MP-α_3C.

Using transient absorption (TA) spectroscopy, we show the light-induced formation of 2MP$^{\bullet}$-C_{32} and 4MP$^{\bullet}$-C_{32} radicals, which are long-lived ($t_{1/2}$ > 100 s) and exhibit different optical and EPR spectra. Calculations show the alternate spin-density distribution patterns typical of neutral (deprotonated) phenol radicals with only minor spin densities on the sulfur atoms. We found that the rate and mechanism by which X_{32} is oxidized are not sensitive to a major change in the phenol OH SASA nor removing the 2MP-C_{32}/E_{13} interaction. Instead, we observed that a 1.6 unit decrease in the phenol pK_a compared to α_3Y is sufficient to alter the oxidation reaction from a pH-dependent, mixed CEPT/PTET mechanism to mainly following a PTET pathway. Interestingly, this pK_a driven change in the X_{32} oxidation mechanism can be reversed by increasing the ΔG°_{ET}. Our results highlight the critical balance between ET and PT driving forces in controlling PCET mechanisms.

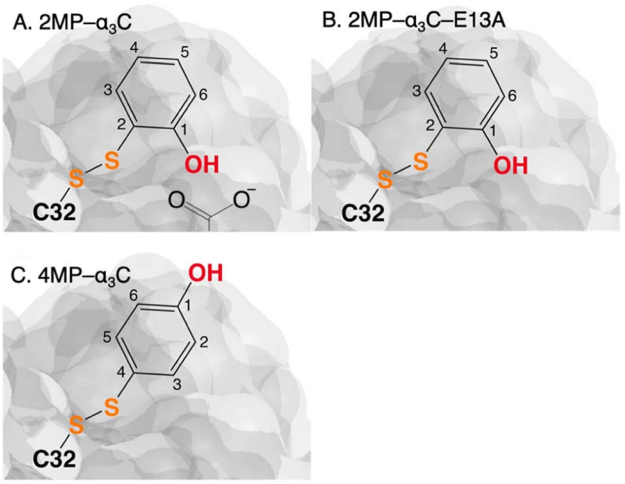

Fig. 1 Schematic description illustrating the protein design and key differences between the MP-C_{32} site in (A) 2MP-α_3C, (B) 2MP-α_3C-E_{13}A, and (C) 4MP-α_3C. Modified with permission from ref. 14 Copyright © 2013 American Chemical Society.

Materials and methods

Transient absorption sample preparation

2MP- and 4MP-α_3C were prepared as described earlier[14] and stored as lyophilized protein powder. Lyophilized protein was dissolved in 100 mM phosphate buffer KP_i (KH_2PO_4 from Sigma Life Science ≥99% purity, K_2HPO_4 from ACROS Organics 99%+ purity), containing 40 mM KCl (Alfa Aesar 99.0–100.5% purity). In experiments where rate constants were measured as a function of buffer concentration, the following concentrations were used: [KP_i], 20–400 mM; [2MP-α_3C], 320–360 μM; [4MP-α_3C], 240 μM; $[Ru(bpy)_3]Cl_2$, 20–30 μM; and $[Co(NH_3)_5Cl]Cl_2$, 3–5 mM. In experiments where rate constants were measured as a function of pH, the following concentrations were used: [KP_i], 100 mM; [2MP-α_3C,] 240–390 μM; [4MP-α_3C], 170–540 μM; [2MP-α_3C-E_{13}A], 330 μM; $[Ru(bpy)_3]Cl_2$, 20-30 μM; $[Ru(dmb)_3]Cl_2$, 20–30 μM; $[Ru(deeb)_3]Cl_2$, 20–30 μM; $[Co(NH_3)_5Cl]Cl_2$, 4–6 mM; and $[Na_2S_2O_8]$, 5 mM. Protein, photosensitizer and quencher concentrations were determined spectrophotometrically using a Cary 50 UV-vis spectrometer and extinction coefficients: ε_{290}(2MP-α_3C) 3700 M^{-1} cm^{-1};[9] ε_{290}(4MP-α_3C) 2300 M^{-1} cm^{-1};[9] ε_{452}($[Ru(bpy)_3]^{2+}$) 14 600 M^{-1} cm^{-1};[15] ε_{460}($[Ru(dmb)_3]^{2+}$) 14 600 M^{-1} cm^{-1};[15] ε_{464}($[Ru(deeb)_3]^{2+}$) 23 300 M^{-1} cm^{-1};[15] ε_{532}-($[Co(NH_3)_5Cl]^{2+}$) 52 M^{-1} cm^{-1}.[12] Photosensitizer and quencher solutions were always prepared separately and mixed under dark conditions. For the α_3X samples, the protein was added to the photosensitizer solution prior to mixing with the quencher solution. The solution pH was adjusted with 0.1–1 M NaOH and

0.01–1 M HCl and measured using a calibrated Metrohm LL Biotrode pH-electrode.

Transient absorption methods

The TA laser flash-photolysis setup has previously been described in detail.[12,16,17] Briefly, the sample was excited using a Nd:YAG laser (Quantel, BrilliantB) with the laser light passed through an OPO tuned to 460 nm. Care was taken to avoid probe-light photochemistry during each experiment, and irreversible photoconversion of the sample by ambient, laser or probe light prior to the actual experiment. The probe light was first passed through a monochromator (Applied Photophysics, pbp Spectra Kinetic Monochromator 05-109 with slit widths set to 4 mm in and out) before hitting the sample at a 90° angle relative to the excitation light. After the sample, the probe light was passed through a 2nd monochromator (same model as listed above with slit widths set to 2 mm in and out) before reaching the PMT detector (Hamamatsu R928). The signal was digitized in a digital oscilloscope (Agilent Technologies Infiniium 600 MHz). TA traces were produced with the Applied Photophysics LKS software package. The laser power was 10–13 mJ per shot. TA spectra were recorded on a UV-vis spectrometer (Agilent 8453 diode array). The sample was excited using a 447.5 nm LED (Luxeion Star, Rebel premounted LED fitted with carlco 29.8/10 mm lens) controlled by an HP 8116A 50 MHz pulse/function generator to supply a reproducible pulse length of 500 ms.

TA samples were contained in a 4 × 10 mm cuvette with an extra-long neck to avoid losing sample during deoxygenation. For the flash-photolysis measurements, the probe light was led through the 10 mm pathlength, and for the TA spectra, the probe light was led through the 4 mm pathlength. When $[Co(NH_3)_5Cl]Cl_2$ was used as the quencher, oxygen was excluded from the sample by gently purging with high purity Ar gas for 10 minutes. When $Na_2S_2O_8$ was used as the quencher, oxygen was not removed. All experiments were carried out at 23 (±1) °C.

Changes in pH of *ca.* 0.1–0.2 units were observed for flash-photolysis samples. The pH was therefore measured before and after TA, and the average values reported here.

Solution NMR spectroscopy

^{13}C,^{15}N-α_3C expression and purification, MP labeling, and NMR sample preparations were conducted as described previously.[14,18] Standard multidimensional NMR experiments were conducted at 30 °C using a 750 MHz Bruker Avance III spectrometer equipped with a cryoprobe. ^1H, ^{13}C, and ^{15}N resonance assignments were made as described in ref. 14 and 18. NOE-based distance restraints were obtained as described in ref. 18. NMR data were processed with Felix95 (Accelrys Inc., San Diego, CA) and analyzed with SPARKY.[19] Structural calculations were performed with the CNS software suite,[20] as described in ref. 12. SASA analyses were perform with MOLMOL.[21] Structural coordinates (RCSB Protein Data Bank ID 8VSW) and NMR chemical shifts (Biological Magnetic Resonance Data Bank, BMRB ID 31067) have been deposited for 4MP-α_3C.

X-band EPR spectroscopy

All electron paramagnetic resonance spectra were recorded on a Bruker EMX-micro spectrometer equipped with an EMX-Primium bridge and an ER4119HS resonator. Individual solutions were deoxygenated before mixing and the final sample concentrations were 230–250 μM protein, 20–30 μM $[Ru(bpy)_3]^{2+}$, and 4.5 mM $[Co(NH_3)_5Cl]^{2+}$. Each sample was ~100 μL and contained in a flat cell. A dark spectrum was recorded before the sample was exposed to *in situ* continuous illumination of a 447.5 nm LED (same setup as above) at ambient atmosphere. EPR settings: microwave frequency, 9.85 GHz; microwave power 6.3 mW; modulation frequency 100 kHz; modulation amplitude 0.1 mT. The Xepr software package (Bruker) was used for data acquisition and processing.

Computational studies

Geometry optimizations were performed using density functional theory (DFT) with Gaussian 16.[22] The DFT calculations used the B3LYP-D3(BJ),[23,24] ωB97X-D,[25] and M06-2X[26] density functionals and various basis sets as specified. In addition, complete active space self-consistent field (CASSCF) calculations were performed with the aug-cc-pVTZ basis set[27,28] using the PySCF program[29,30] for geometries optimized at the DFT ωB97X-D/6-31+G** level. The active spaces were chosen with the automated π-orbital space (PiOS) method,[31] which constructed a (9e, 8o) active space for the 4MP and 2MP models and a (7e,7o) active space for the Y model. Mulliken spin population analyses were conducted for the various radical systems.

To investigate H-bonding interactions, classical molecular dynamics (MD) simulations of the 2MP-α_3C and 4MP-α_3C proteins were performed with Amber20 (ref. 32) using the ff14SB forcefield[33] with TIP3P water.[34] The simulation protocol was similar to our previous computational studies on α_3Y proteins.[13] Detailed H-bonding analyses were conducted for 1 microsecond trajectories. An additional 5 ps quantum mechanical/molecular mechanical (QM/MM) trajectory was also propagated. Complete computational details are provided in the ESI.†

Results and discussion

Site 32 in α_3Y, 2MP-α_3C and 4MP-α_3C

The α_3X system was designed to sequester X_{32} and thereby isolate and stabilize the $X_{32}^{\bullet}$ state. NMR spectroscopy has been used to obtain high-quality solution structures of α_3X proteins, including α_3Y (RCSB PDB ID 2MI7), 2MP-α_3C (2LXY) and 4MP-α_3C (this study, see ESI† page S9 for experimental restraints and structural statistics). Y_{32} displays effectively no SASA (0.2 ± 0.2%) and resides at an average depth of 7.7 ± 0.3 Å below the protein surface.[12] The MP-α_3C proteins were designed to modulate the exposure of the phenol OH while minimizing other structural changes, both globally to the α_3 scaffold and locally to the radical site.[9] As illustrated in Fig. 2, the MP-α_3C structures confirm this very detailed design and show that the phenol OH SASAs for 2MP-α_3C and 4MP-α_3C differ by around one order of magnitude.

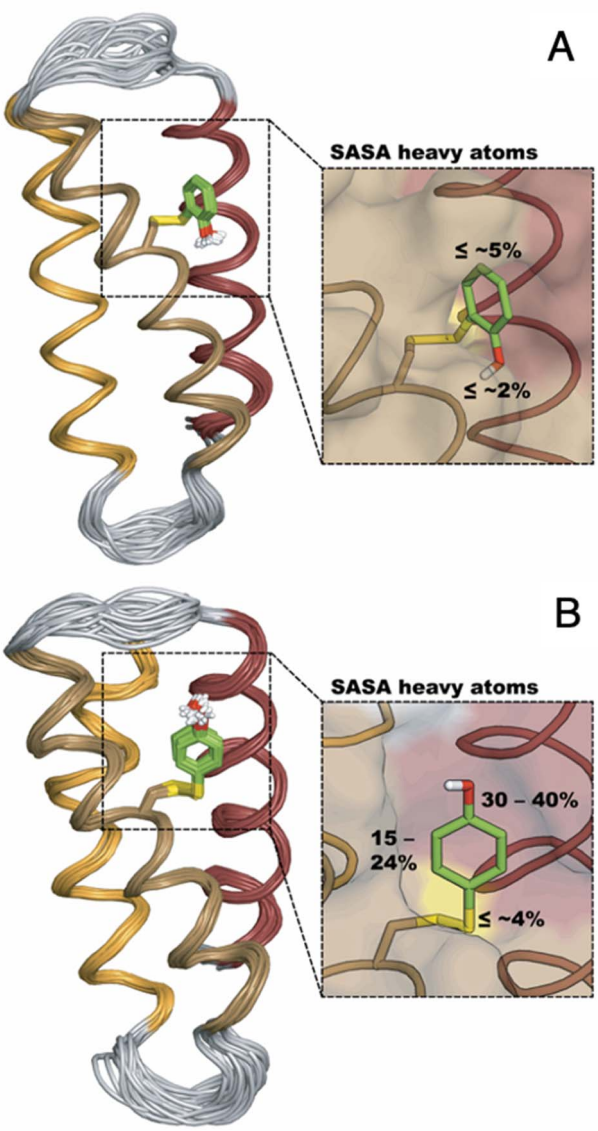

Fig. 2 Ribbon diagram representations of the (A) 2MP-α_3C (RCSB PDB ID 2LXY) and (B) 4MP-α_3C (8VSW) solution NMR structures. The average SASA of 2MP-C_{32} and 4MP-C_{32} are 3.5 ± 0.7% and 8.7 ± 2.4%, respectively, across the 32-member structural ensembles that represent these proteins in solution. The zoom-in panels display the ensemble average SASA of the heavy atoms in the MP-C_{32} residues. Top panel, SASA of 2MP-C_{32}: aromatic C_1 carbon and phenol oxygen, ≤~2%; all other heavy atoms, ≤~5%. Bottom panel, SASA of 4MP-C_{32}: aromatic C_1 carbon and phenol oxygen, 30–40%; all remaining aromatic carbons, 15–24%; S–S bridge and C_{32} atoms, ≤~4%. The percent SASA given for the heavy atoms are relative to the total area of each individual atom.

Fig. 3 shows the five hydrophilic residues that form part of the MP-C_{32} radical sites. We observe no obvious protein residue that may serve as the primary proton acceptor upon 4MP-C_{32} oxidation. Water and/or buffer species appear more likely. In contrast, the 2MP-C_{32} phenol O and the E_{13} carboxylate group reside at an average distance consistent with a weak H-bond (O–O distance = 3.2 ± 0.5 Å). We hypothesized that the presence of a H-bond could facilitate PT to E_{13} upon 2MP-C_{32} oxidation. To investigate this further, PCET rate constants were determined for 4MP-α_3C and 2MP-α_3C ± E_{13} (*vide infra*).

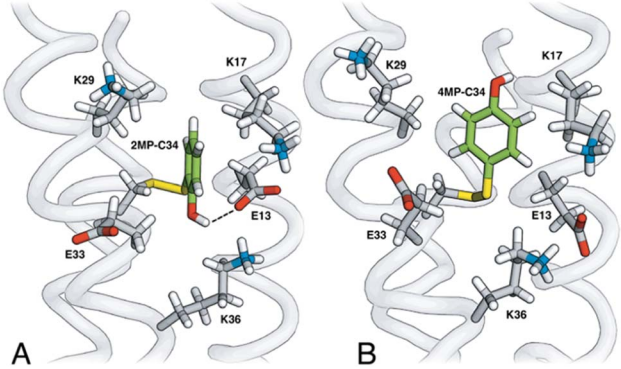

Fig. 3 Site 32 in (A) 2MP-α_3C and (B) 4MP-α_3C consist of atoms from hydrophobic amino acids (not shown) and five hydrophilic residues, K_{17}, K_{29}, K_{36}, E_{13} and E_{33}. The phenol OH points toward (2MP-C_{32}) or away from (4MP-C_{32}) the carboxylate groups of E_{13} and E_{33}. Analysis of the 2MP-α_3C structure provides a phenol O to glutamate O distance of 3.2 ± 0.5 Å and 7.2 ± 0.2 Å for the 2MP-C_{32}/E_{13} and 2MP-C_{32}/E_{33} pair, respectively.

Table 1 summarizes relevant thermodynamic properties of the MP-α_3C proteins relative to the α_3Y reference with protein. $E^{o\prime}(X_{32}^{\bullet}/X_{32})$ of 2MP-α_3C and 4MP-α_3C are 54 ± 3 and 175 ± 10 mV less oxidizing relative to α_3Y between pH 5.0 and 10.[5] The MP-C_{32} residues exhibit pK_a values that are 1.6–2.1 units below the pK_a of Y_{32}. 2MP-α_3C has a higher pK_a value than the other MP-α_3C proteins, likely because of stabilization from H-bonding to E_{13}. In the absence of this interaction, the pK_a of the phenol OH decreases by 0.5 units.

Radical formation and decay in MP-α_3C

Radical formation and decay were followed by TA spectroscopy. The Ru^{3+} oxidant was formed *in situ via* the flash-quench method[12,13,17,35] on samples containing MP-α_3C protein, photosensitizer ($[Ru(L)_3]^{2+}$, L = 4,4′-R_2-2,2′-bipyridine, R = –H $[Ru(bpy)_3]^{2+}$, $-CH_3$ $[Ru(dmb)_3]^{2+}$, or $-COOC_2H_5$ $[Ru(deeb)_3]^{2+}$, Scheme 1), and quencher ($[Co(NH_3)_5Cl]^{2+}$ or persulfate ($Na_2S_2O_8$)). The photosensitizers used here span a ΔE^{o} range of *ca.* 440 mV: $E^{o}([Ru(dmb)_3]^{3+/2+}) = 1100$ mV, $E^{o}([Ru(bpy)_3]^{3+/2+}) = 1260$ mV, and $E^{o}([Ru(deeb)_3]^{3+/2+}) = 1540$ mV; all values reported *vs.* the NHE, see ESI† page S7 for details).[15] The estimated error for each absolute $E^{o}(Ru^{3+/2+})$ value is ~±30 mV. For radical formation kinetics, a 10 ns laser flash at 460 nm was

Table 1 α_3X midpoint reduction potentials, $E^{o\prime}$, and pK_a values ± SD[a]

	$E^{o\prime}(X_{32}^{\bullet}/X_{32})$/mV			
Protein	At pH 5.5	At pH 8.5	$E^{o}(X_{32}^{\bullet}/X_{32}^{-})$ mV[b]	pK_a
α_3Y	1065 (±2)	904 (±3)	749 (±4)	11.3 (±0.1)
2MP-α_3C	1011 (±3)	847 (±2)	780 (±4)	9.7 (±0.2)[c]
4MP-α_3C	890 (±10)	715 (±10)	654 (±10)	9.5 (±0.1)
2MP-α_3C-E_{13}A	—	—		9.2 (±0.2)[c]

[a] Potentials (*vs.* NHE) and pK_a values were obtained from ref. 5. [b] Determined from α_3X Pourbaix diagrams[5] at pH >> pK_a of reduced X_{32}. [c] Determined in the present work (Fig. S1 and S2).

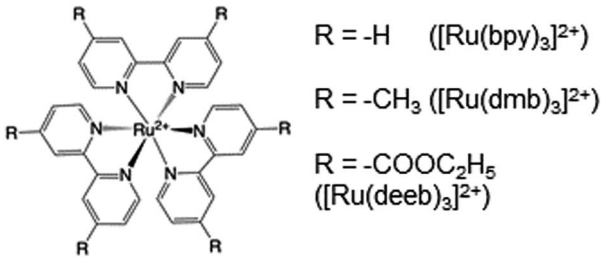

Scheme 1 Chemical structure of employed ruthenium tris-4,4′-R-2,2′-bipyridine photosensitizers.

used to excite the photosensitizer, which in turn was oxidatively quenched to form $[Ru(L)_3]^{3+}$. The PCET reaction leading to radical formation was followed at 410 and 450 nm, monitoring $[Ru(L)_3]^{2+}$ ground state bleach recovery concomitant with the growth of radical absorption (Fig. 4B and E). The 410 and 450 nm traces were well fitted with single-exponential functions, following a pseudo-first order dependence on the concentration of $[Ru(L)_3]^{3+}$, with MP-α_3C in excess (*vide infra*). Note that without protein, the $[Ru(L)_3]^{2+}$ ground state bleach was stable on the time scale examined (grey data in Fig. 4B and E). For radical spectra and decay kinetics, a 500 ms LED pulse was instead used to excite the photosensitizer, which was quenched by $[Co(NH_3)_5Cl]^{2+}$.

Fig. 4 shows TA spectra and radical formation and decay kinetics for 2MP-α_3C (top row) and 4MP-α_3C (bottom row). We note that previous protein film voltammetry (PFV) and TA studies have shown that the α_3 scaffold is unreactive, even at highly oxidizing conditions.[7,8,12–14,17] PFV characterization of α_3X proteins containing Y or Y analogs show fully reversible $X_{32} \leftrightarrow X_{32}^{\bullet} + H^{+}$(bulk) redox cycles.[7,8,10,11,14] This is due to the large redox-induced pK_a shifts of phenols, with the pK_a of the cation radical typically <0.[36] The TA spectra shown in Fig. 4A and D are thus assigned to the neutral 2MP$^{\bullet}$-C_{32} and 4MP$^{\bullet}$-C_{32} radicals, respectively. Consistent with this conclusion, the 2MP$^{\bullet}$-C_{32} spectra are reminiscent of $Y_{32}^{\bullet}$ spectra recorded under similar conditions,[12] while the 4MP$^{\bullet}$-C_{32} spectra share spectral similarities with the neutral 4-hydroxythiophenoxyl radical.[37]

Radical decay kinetics were extracted by plotting the change in radical absorption (380 nm for 2MP-α_3C and 500 nm for 4MP-α_3C) as a function of time. A fit to second order kinetics was used to calculate the first half-life, $t_{1/2}$, where $t_{1/2} = 1/(k_2 Abs_0(\text{-MP}^{\bullet}\text{-}C_{32}))$. This analysis provided $t_{1/2}$(2MP$^{\bullet}$-C_{32}) = 100 s, $t_{1/2}$(4MP$^{\bullet}$-C_{32}) = 130 s, and $t_{1/2}$(2MP$^{\bullet}$-C_{32} in 2MP-α_3C-E_{13}A) = 24 s (Fig. S10†). Extinction coefficients are not known for these radicals, but we estimated the initial concentrations, and thus calculated the rate constants. From the initial Ru^{2+} ground state

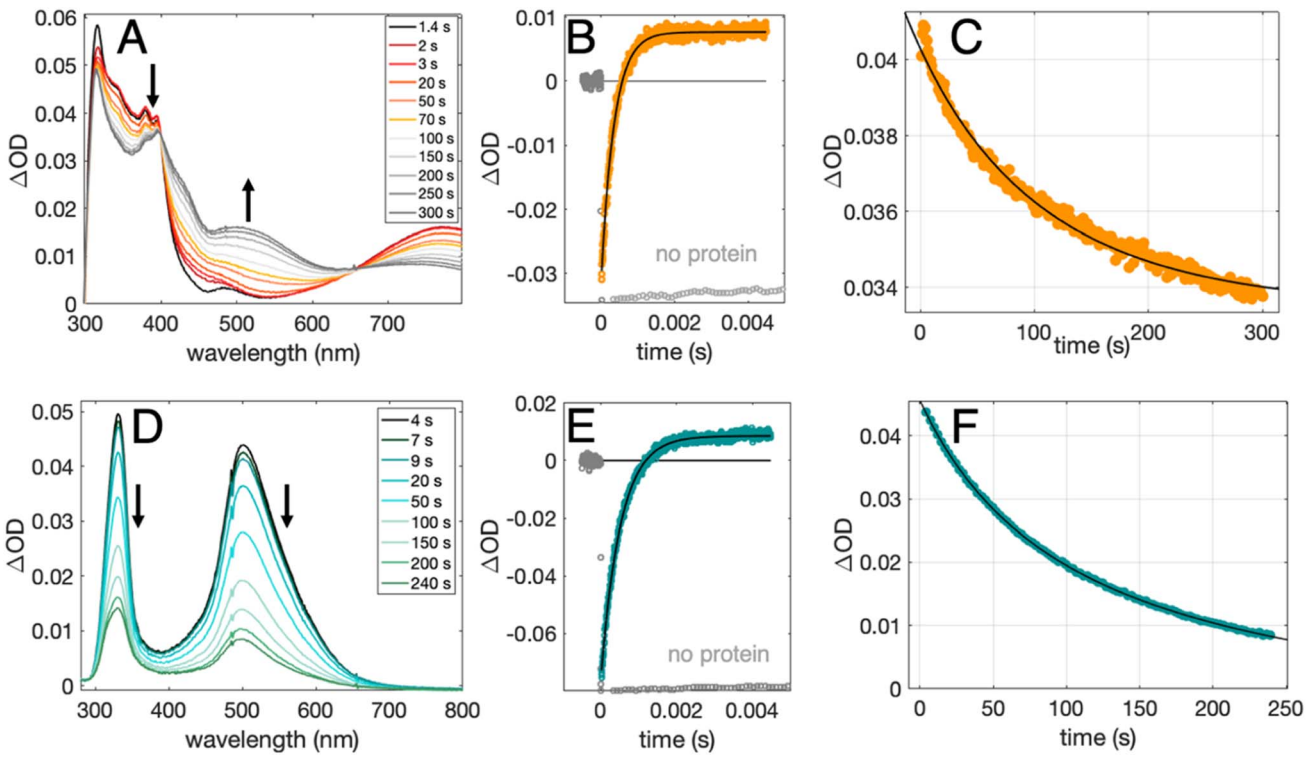

Fig. 4 TA spectra, formation kinetics traces, and decay kinetics traces for 2MP$^{\bullet}$-C_{32} (top row) and 4MP$^{\bullet}$-C_{32} (bottom row). (A and D): TA difference spectra recorded at pH 6.5 (±0.1) following a 500 ms 447.5 nm LED pulse. (B and E): TA kinetic traces recorded at pH 8.5 (±0.1) following a 10 ns laser pulse at 460 nm, monitored at 410 nm (2MP-α_3C, orange) or 450 nm (4MP-α_3C, green), and single-exponential fits (black) following the oxidation of MP-C_{32} by $[Ru(bpy)_3]^{3+}$; traces without protein are shown in gray. (C and F): decay kinetics recorded at pH 6.5 (±0.1) following a 500 ms 447.5 nm LED pulse, monitored at 380 nm (2MP$^{\bullet}$-α_3C), and 500 nm (4MP$^{\bullet}$-α_3C), where black lines show second-order fits. Samples contained 230-590 μM protein, 30 μM $[Ru(bpy)_3]^{2+}$, and 4–5 mM $[Co(NH_3)_5Cl]^{2+}$.

bleach and final radical signal in Fig. 4B and E, and assuming ~100% conversion to the radicals, the initial radical concentration is ~13 μM in the experiments with pulsed diode excitation (Fig. 4A, C, D and F; see ESI† for details). This estimate gives rate constants for radical–radical decay of $k_2 \approx 80$, 60 and 300 M^{-1} s^{-1} for 2MP$^{\bullet}$-C_{32}, 4MP$^{\bullet}$-C_{32}, and 2MP$^{\bullet}$-C_{32} in 2MP-α_3C-E_{13}A, respectively. Both 2MP$^{\bullet}$-C_{32} and 4MP$^{\bullet}$-C_{32} give rise to optical features that persisted for more than 200 s. This provided the opportunity to collect EPR spectra, as describe below.

Characterization of the 2MP-α_3C and 4MP-α_3C radicals

The distinct UV-vis spectra shown in Fig. 4A and D suggest that 2MP$^{\bullet}$-α_3C and 4MP$^{\bullet}$-α_3C have significantly different electronic structures. To support the notion that each UV-vis spectrum represents a single major radical species, we used EPR spectroscopy to further characterize MP-α_3C under photo-oxidizing conditions. EPR spectra were collected from MP-α_3C dissolved in 100 mM KP_i, 40 mM KCl pH 6.5 buffer, and using $[Ru(bpy)_3]^{2+}$ as the photosensitizer and $[Co(NH_3)_5Cl]^{2+}$ as the quencher. The experiments were conducted at room temperature under constant illumination by a 447.4 nm LED lamp. A strong paramagnetic signal was observed to rise when the LED lamp was switched on and to subsequently decay when the LED lamp was switched off. No signal was observed prior to illumination. The EPR spectra representing the light-induced 2MP$^{\bullet}$ and 4MP$^{\bullet}$ species are shown in Fig. 5A and B, respectively. The spectra are consistent with the primary radicals 2MP$^{\bullet}$ and 4MP$^{\bullet}$. The former give rise to a hyperfine pattern due to hydrogen nuclear spin of four inequivalent protons, while the latter contains two equivalent proton pairs. As expected, the widths of the MP-α_3C spectra are narrow relative to a typical protein Y$^{\bullet}$ spectrum. The MP-C_{32} residues lack β-methylene protons (Fig. 1), which have a major geometry-dependent impact on the linewidth of a Y$^{\bullet}$ spectrum.[38]

The radical spin distribution was investigated using both DFT and multireference methods. The spin densities were calculated for optimized geometries of the 2MP-α_3C, 4MP-α_3C, and α_3Y side chain analogs in their neutral and cationic radical states using unrestricted DFT and CASSCF calculations. Spin densities were visualized, and the Mulliken spin population[39] values were computed. These are provided for the CASSCF/aug-cc-pVTZ computations in Fig. 6 and Table 2. Fig. 6 shows the expected alternating pattern of α and β spin density in the aromatic ring for neutral radicals, with cationic radicals having less spin density on the oxygen and being more delocalized over the aromatic ring. This behavior is quantified in Table 2 through Mulliken spin population analysis. These trends show that the neutral radical 4MP$^{\bullet}$ has slightly more spin on the sulfur atoms than 2MP$^{\bullet}$, but this effect is much more pronounced in the radical cation forms. Values for the spin populations computed for the Y neutral and cationic radicals are also provided as a reference. These trends were also observed for DFT calculations using three different functionals, namely B3LYP-D3(BJ),[23,24,40] ωB97X-D,[25] and M06-2X,[26] with the 6-31G** and 6-31+G** basis sets for all three functionals and additionally the 6-31++G** basis set[41–43] for the ωB97X-D functional (see ESI†). We conclude that for the neutral radicals there

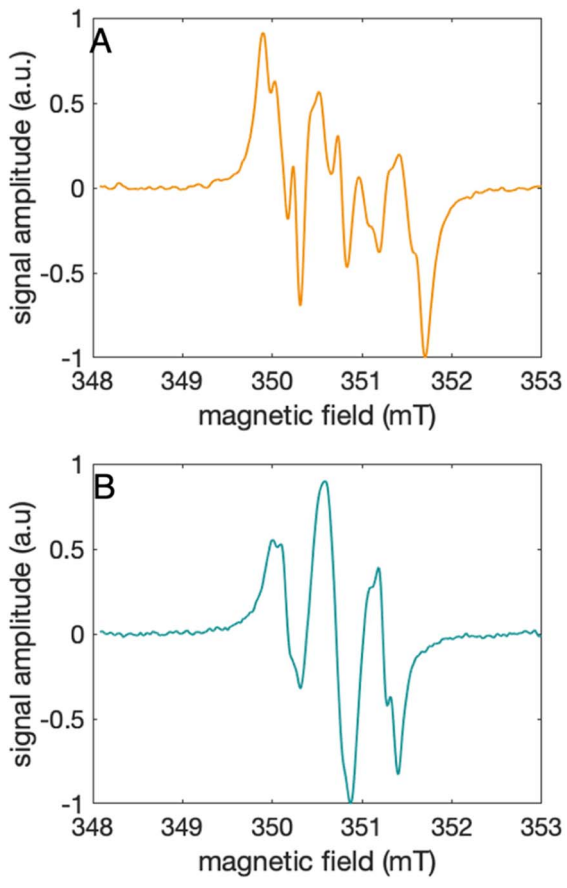

Fig. 5 EPR spectra collected at ambient temperature under continuous illumination using a 447.5 nm LED of (A) 2MP-α_3C, shown in orange, and (B) 4MP-α_3C, shown in green. EPR settings: microwave frequency, 9.85 GHz; microwave power 6.3 mW; modulation frequency 100 kHz; modulation amplitude 0.1 mT.

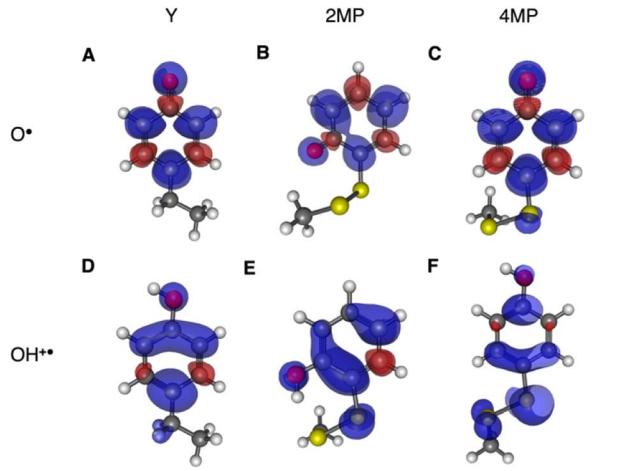

Fig. 6 Spin densities computed with CASSCF/aug-cc-pVTZ for neutral radicals (A–C) and cationic radicals (D–F) with an isovalue of 0.002 $Å^{-3}$. Analogous plots for DFT are provided in the ESI.†

Table 2 Mulliken spin populations on key atoms of side chain analogs of the redox-active side chain in 2MP-α_3C and 4MP-α_3C calculated with CASSCF/aug-cc-pVTPZ

	Atom[a]			
System	O	S	S_2	Total S[b]
Y–O$^{\bullet}$	0.340	—	—	—
2MP-O$^{\bullet}$	0.310	0.013	0.006	0.019
4MP-O$^{\bullet}$	0.321	0.049	0.002	0.051
Y–OH$^{+\bullet}$	0.106	—	—	—
2MP-OH$^{+\bullet}$	0.120	0.105	0.003	0.108
4MP-OH$^{+\bullet}$	0.041	0.453	0.078	0.531

[a] O refers to the hydroxyl oxygen of the sidechain, S refers to the sulfur atom closest to the phenol ring, and S_2 refers to the sulfur atom most distal to the phenol ring, *i.e.*, closest to the backbone. [b] "Total S" refers to the total spin population on the sulfur atoms in the molecule. A full set of data is available in the ESI for all theoretical methods used in this study.

is very little spin density on the sulfur atoms that ligate the phenols to the α_3 scaffold (we note that early calculations suggested a larger spin density on the sulphur).[37] Our results strengthen the use of MPs as a model system for canonical protein Y redox sites.

pH-dependent rate constants for radical formation

PCET rate constants (k_{PCET}) reflecting MP-C_{32} oxidation by $Ru(L)_3^{3+}$ were obtained as a function of buffer concentration (Fig. S5†), pH, and ΔG°_{ET} (Fig. 7 and 8; Table 3). ΔG°_{ET} was modulated by using the three photosensitizers shown in Scheme 1 ($\Delta E^{\circ}(Ru^{(3+/2+)})$ *ca.* 440 mV, *vide supra*). In all experiments, the protein concentration was much higher

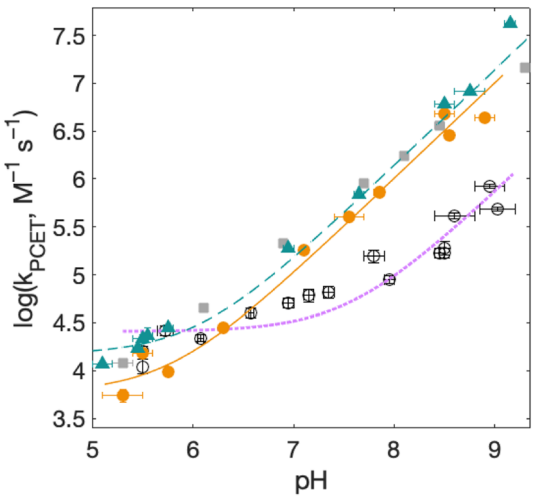

Fig. 7 Rate constants for radical formation *vs.* pH using $[Ru(bpy)_3]^{3+}$ as oxidant for 2MP-α_3C (orange dots), 2MP-α_3C-E_{13}A (grey squares), and 4MP-α_3C (green triangles), compared to previously published data for α_3Y (black circles).[13] Standard deviations are shown, but are often smaller than the size of the data symbols. Samples contained 60–620 μM protein, 30 μM $[Ru(bpy)_3]^{2+}$, and 4–6 mM $[Co(NH_3)_5Cl]^{2+}$. Fits according to eqn (1) are shown as lines (see Table 4 for results).

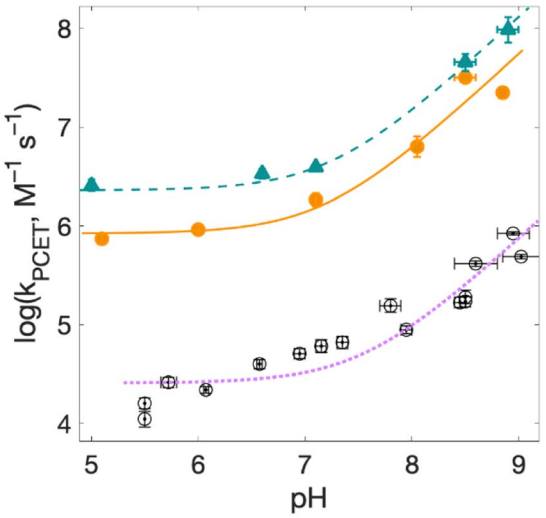

Fig. 8 Rate constants for radical formation as a function of pH for 2MP-α_3C (orange dots) and 4MP-α_3C (green triangles), with $[Ru(deeb)_3]^{3+}$ as oxidant, and α_3Y (black circles, fit with a purple dotted line curve) with $[Ru(bpy)_3]^{3+}$ as oxidant from ref. 13, other conditions as in Fig. 7. Standard deviations are shown, but are often smaller than the size of the data symbols. Fits according to eqn (1) are shown (see Table 4 for results).

Table 3 PCET rate constants at pH 5.5 and 8.5 for 2MP-α_3C and 4MP-α_3C with $[Ru(L)_3]^{3+}$ oxidants and their $Ru^{3+/2+}$ potentials

Oxidant	pH	k_{PCET} (M^{-1} s^{-1})	E°[a] (mV *vs.* NHE)
2MP-α_3C			
$Ru(dmb)_3^{3+}$	5.5(±0.1)	2.8×10^3	+1100
$Ru(bpy)_3^{3+}$	5.5(±0.1)	1.5×10^4	+1260
$Ru(dmb)_3^{3+}$	8.5(±0.1)	7.7×10^5	+1100
$Ru(bpy)_3^{3+}$	8.5(±0.1)	4.8×10^6	+1260
$Ru(deeb)_3^{3+}$	8.5(±0.1)	3.2×10^7	+1540
4MP-α_3C			
$Ru(dmb)_3^{3+}$	5.5(±0.1)	4.4×10^3	+1100
$Ru(bpy)_3^{3+}$	5.5(±0.1)	2.1×10^4	+1260
$Ru(dmb)_3^{3+}$	8.5(±0.1)	1.5×10^6	+1100
$Ru(bpy)_3^{3+}$	8.5(±0.1)	6.1×10^6	+1260
$Ru(deeb)_3^{3+}$	8.5(±0.1)	5.4×10^7	+1540

[a] Error bars are estimated to be ±30 mV.

(200–600 μM) than the concentration of the *in situ* generated Ru^{3+} oxidant (1–6 μM), resulting in pseudo-first order kinetics for radical formation. To confirm that the reactions were first order with regards to [protein], rate constants were also determined as a function of [protein] at one or two pH values for each oxidant (Fig. S4, S7, and S9; see ESI† for details). The large excess of protein also resulted in complete consumption of $[Ru(L)_3]^{3+}$, with no significant remaining Ru^{2+} bleach. Thus, the reverse reaction could be ignored even for the reactions where $\Delta G^{\circ} \approx 0$ and the observed rate constant can be identified as the forward rate constant for PCET, k_{PCET} (see General discussion).

There is no significant change in k_{PCET} derived from 2MP-α_3C and 4MP-α_3C samples containing 20 to 400 mM KP_i

(Fig. S5†). This observation shows that a buffer species does not serve as the primary acceptor of the phenolic proton as 2MP-C_{32} or 4MP-C_{32} is oxidized. These results agree with results for α_3Y, where buffer species were shown to not participate in the PCET reaction,[13] but stand in stark contrast to results obtained for small molecule Y and W derivatives in solution, where common buffers may be the primary acceptor even at moderate concentrations ($\gtrsim$10 mM).[44,45]

Fig. 7 shows k_{PCET} as a function of pH using $[Ru(bpy)_3]^{3+}$ as the oxidant for 2MP-α_3C (orange), 2MP-α_3C-E_{13}A (grey), and 4MP-α_3C (green) compared to previously published data on α_3Y (black/purple). Kinetic data for all proteins are fit with eqn (1) (below), and the resulting k_{PCET} values are given in Table 4.

$$k_{PCET} = k_{YOH} + k_{YO^-} \times 10^{(pH\text{-}pK_a)} \quad (1)$$

For α_3Y, the first, pH-independent term that dominates at low pH is assigned to a concerted CEPT reaction with water as the primary proton acceptor.[13] The second term is assigned to pre-equilibrium PTET ($PTET_{pre\text{-}eq}$) with the equilibrium fraction of the Y–O^- species increasing ten-fold per pH unit. For MP-α_3C, the contribution of the first term is very small and is only noticeable as a weak pH dependence for the lowest pH data points. As shown in the next section, the mechanisms can be assigned in complete analogy to the α_3Y system: CEPT with H_2O as proton acceptor at the lowest pH values, and PTET at the higher pH values.

Assigning the PCET mechanisms

The kinetic isotope effect (KIE) on PCET rates was determined at 2–3 different pL (L = H or D) values using $[Ru(bpy)_3]^{3+}$ as oxidant. The observed KIE values were significant: 2.9 (pL 6.0 ± 0.1) and 3.6 (pL 9.0 ± 0.1) for 2MP-α_3C, and 6.2 (pL 5.3 ± 0.3), 11.2 (pL 6.3 ± 0.1), and 13.5 (pL 8.6 ± 0.1) for 4MP-α_3C. The large KIE values confirm that PT is part of the rate-limiting step. From these KIEs, we can exclude an ET-limited ETPT reaction over the entire pH range examined. We can also exclude a pre-equilibrium ETPT because this mechanism requires that the pre-equilibrium is faster than the subsequent reaction, which is highly improbable given that the pK_a's of phenols typically drop to values <0 upon oxidation.[36]

A pH-independent PTET reaction at low pH can be excluded because deprotonation of weak acids to water (H_2O) is slow: k_{PT} ~100 s^{-1} for pK_a = 9,[46] which is much slower than our observed first-order rate constants. Other potential proton acceptors (OH^-, buffer) increase in concentration as the pH increases and would not have given a pH-independent rate constant. This analysis suggests that the pH-independent reaction is CEPT with H_2O as the primary proton acceptor.

The pH-dependent rate constants (second term in eqn (1)) can have two origins. First, for a $PTET_{pre\text{-}eq}$ mechanism, the pre-equilibrium shifts with pH because at higher pH values there is a larger fraction of already deprotonated species, which leads to faster rate constants. Second, for an irreversible reaction step (CEPT or PT-limited PTET), the concentration of the proton-accepting species can depend on pH, which would be the case for *e.g.* OH^- and base forms of the buffer. At high pH, CEPT with OH^- as the primary proton acceptor can most likely be excluded because the observed (pseudo-first order) rate constants are too large to be explained by a diffusional reaction with the $[OH^-]$ present in the solution in the pH interval studied, see ESI page S12.† The PT-limited PTET could be excluded by comparing the rate constants with those obtained with a weaker oxidant, namely $[Ru(dmb)_3]^{3+}$ at pH 5.5 ± 0.1 and 8.5 ± 0.1 (Table 3). Both 2MP-α_3C and 4MP-α_3C showed slower rate constants with the weaker oxidant. This is inconsistent with a PT-limited reaction but is consistent with $PTET_{pre\text{-}eq}$, for which the overall rate constant depends also on the rate constant for the second step. This analysis suggests that 2MP-α_3C and 4MP-α_3C oxidation by $[Ru(bpy)_3]^{3+}$ (Fig. 7) proceeds mainly *via* a $PTET_{pre\text{-}eq}$ mechanism, with CEPT dominating only at the lowest pH values. Note that we can exclude a significant contribution from the reverse PCET reaction for reactions at $\Delta G^\circ \approx 0$, which could have given a pH-dependence of the net reaction,[47] because we use great excess of protein, making the reaction go to completion in a single kinetic phase ($\Delta G < 0$), and no remaining Ru^{2+} bleach is seen over a large variation of pH values and observed rate constants. Moreover, a parallel pH-dependence is observed also with the strong oxidant $[Ru(deeb)_3]^{3+}$, for which $\Delta G^\circ \ll 0$.

Table 4 Rate constants k_{YOH} and k_{YO^-}[a]

Oxidant	k_{YOH} (M^{-1} s^{-1})	k_{YO^-} (M^{-1} s^{-1})
2MP-α_3C		
$Ru(dmb)_3^{3+}$	—	1.2×10^{7}[b]
$Ru(bpy)_3^{3+}$	5.8×10^{3}	5.1×10^{7}
$Ru(deeb)_3^{3+}$	8.4×10^{5}	2.7×10^{8}
4MP-α_3C		
$Ru(dmb)_3^{3+}$	—	1.5×10^{7}[b]
$Ru(bpy)_3^{3+}$	1.5×10^{4}	4.4×10^{7}
$Ru(deeb)_3^{3+}$	2.3×10^{6}	4.0×10^{8}
α_3Y		
$Ru(bpy)_3^{3+}$	2.6×10^{4}	1.4×10^{8}

[a] From fits according to eqn (1). [b] Calculated from the pH 8.5 value multiplied by $10^{(pK_a-8.5)}$, see text.

Proton transfer is not facilitated by increased solvent exposure nor by a nearby internal proton acceptor

Rate constants determined for 4MP-α_3C are slightly higher compared to those for 2MP-α_3C. This is most likely due to the lower $E^{o\prime}(X_{32}^{\bullet}/X_{32})$ and pK_a values of 4MP-α_3C. As the rate constant difference is modest, it appears that the higher phenol OH SASA of 4MP-C_{32} does not further accelerate PCET. Specifically, it does not seem to facilitate PT to water, and it does not allow sufficient access of buffer for this to be the primary proton acceptor.

The relatively close distance of 2MP and E_{13} in 2MP-α_3C (Fig. 3A) did not lead to any clear increase of the PCET rate constant compared to 4MP-α_3C. Glutamate is a stronger base than water, with pK_a ~4.5 *vs.* 0 for their respective conjugate

acids, and glutamate as a proton acceptor would be expected to accelerate PCET. Moreover, the 2MP-α_3C rate constant is even slightly higher for 2MP-α_3C-E_{13}A, which lacks this glutamate residue (Fig. 7). We can therefore exclude E_{13} as the primary proton acceptor and instead assign water as the likely proton acceptor for 2MP-α_3C, just as for the other proteins.

MD simulations were performed on the MP-α_3C solution NMR structures (Fig. 2) to better understand the H-bonding interaction between the 2MP-C_{32} or 4MP-C_{32} and water, E_{13}, or E_{33} (Fig. 3 and Table S12†). The simulations show that 4MP-C_{32} H-bonds primarily with water and has negligible interaction with E_{13} and E_{33}. 2MP-C_{32} H-bonds with water to a much lesser extent and interacts also with E_{33} but not significantly with E_{13}. Note that the NMR structure does not indicate a H-bond between 2MP-C_{32} and E_{33} (Fig. S21†), within strict distance and angle criteria. Moreover, the H-bond between 2MP-C_{32} and E_{13} is retained in a QM/MM MD trajectory, where the 2MP-C_{32} and E_{13} sidechains are treated with DFT (Fig. S23†). Thus, the preference for H-bonding of 2MP-C_{32} to E_{33} over E_{13} may be due to limitations of the force field, and the QM/MM simulations suggest that 2MP-C_{32} can H-bond to E_{13}. Nevertheless, analysis of the rate constants suggests that although E_{13} is within H-bonding distance to 2MP-C_{32}, other factors such as insufficient proton vibrational wavefunction overlap inhibit PT.

Rate constants for PCET with various oxidation strengths

For solvated small-molecule Y compounds, a stronger oxidant has been shown to change the PCET mechanism from PTET to CEPT.[2] To test whether an external oxidant could change the PCET mechanism in the α_3X protein system, rate constants were determined as a function of pH using the stronger oxidant $[Ru(deeb)_3]^{3+}$ with persulfate as the quencher (Fig. 8; see ESI† for details). This gave much faster PCET rate constants, and a much more prominent contribution from the pH-independent CEPT reaction (first term in eqn (1)). The pH dependence is very similar to what was observed for α_3Y using $[Ru(bpy)_3]^{3+}$ as the oxidant (black data with purple dotted fit in Fig. 8).[13] Fitting the data to eqn (1) yielded rate constants for the protonated and deprotonated fractions of MP-C_{32} (Table 4).

With $[Ru(deeb)_3]^{3+}$ as the oxidant, the rate constants at pH >7 increase with pH, analogous to the data with $[Ru(bpy)_3]^{3+}$. The mechanism can thus be assigned to $PTET_{pre\text{-}eq}$ also with the stronger oxidant; PT-limited PTET and CEPT with OH^- as the proton acceptor can be excluded as for the experiments with $[Ru(bpy)_3]^{3+}$ above. The rate constant k_{YO^-} is higher with $[Ru(deeb)_3]^{3+}$, as expected from the driving force dependence of $Y–O^-$ oxidation (see General discussion below).

Fig. 8 shows PCET rate constants of 2MP-α_3C and 4MP-α_3C with the stronger oxidant $[Ru(deeb)_3]^{3+}$, in comparison to α_3Y using $[Ru(bpy)_3]^{3+}$. The general trend in pH-dependence of PCET rate constants for 2MP-α_3C and 4MP-α_3C *versus* α_3Y is similar, but the rate constants are significantly accelerated in the former. At low pH, the use of a stronger oxidant can favor the ETPT mechanism, and it is important to demonstrate that proton transfer is a part of the rate limiting step. Experiments were therefore repeated in D_2O at pL 5.6(±0.1) with $[Ru(deeb)_3]^{3+}$ as the oxidant, and resulted in KIE ~3 for both 2MP-α_3C and 4MP-α_3C. This large KIE excludes an ET-limited ETPT mechanism and suggests that PCET proceeds *via* CEPT with H_2O as the primary proton acceptor, as was the case with the weaker oxidants. The rate constant is much larger, as can be expected with the much stronger oxidant (see next section). We note that the pH-independent rate constant cannot be explained by formation of an internal H-bond for 2MP-C_{32} since 4MP-C_{32} shows the same behavior without having a nearby protein proton acceptor.

General discussion

Changing the PCET mechanism by tuning the driving force

The recently introduced PCET zone diagrams[1] can help to visualize which mechanism dominates a PCET reaction, depending on the driving force for initial ET or PT (represented by ΔE° and ΔpK_a, respectively), see Fig. 9. The diagrams assume a Marcus-type free-energy dependence of the rate constant for each mechanistic step (ET, PT or CEPT; see eqn (2) below). The size and shape of each of the mechanistic regions are dictated by the relative pre-exponential factor and reorganization energies for each mechanism.[1] The schematic zone diagram in Fig. 9 has a large CEPT region, which is a result of two factors. First, a large energetic interdependence of ET and PT, manifested by a large difference in $E^\circ(X_{32}^{\bullet+}/X_{32})$ *vs.* $E^{\circ\prime}(X_{32}^{\bullet}/X_{32}^{-})$ and a correspondingly large difference in the phenol pK_a of oxidized and reduced X_{32}, favors a CEPT mechanism under a wide range of conditions. Secondly, a large vibronic coupling between the reactant and product state for CEPT allows for a high probability of electron and proton tunneling. With sufficient kinetic

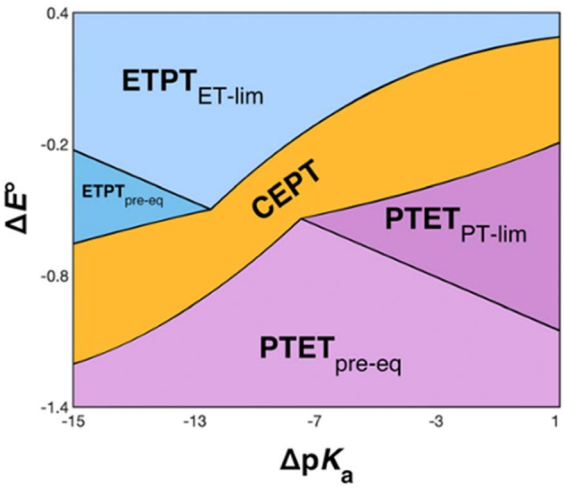

Fig. 9 Schematic zone diagram for a PCET oxidation of a compound HA to A$^\bullet$, where the reaction exhibits a sufficiently large vibronic coupling that CEPT can compete in this range of ΔE° and ΔpK_a values. The axes are defined as $\Delta E^\circ = E^\circ$(oxidant) − $E^\circ(HA^{\bullet+}/HA)$ (in units of volts) and $\Delta pK_a = pK_a(H^+$ base) − pK_a(HA), so that the overall driving force for PCET increases when moving upwards and to the right in the diagram. Adapted with permission from ref. 1. Copyright © 2021 American Chemical Society.

data as a function of ΔE° and ΔpK_a for a system, the lines dividing the zones can be quantitatively estimated.[48]

For bimolecular PCET reactions, bases and oxidants of different strengths can be used to access different PCET regions. However, the protein shields the X_{32} pocket and excludes negatively charged buffer species. This is evidenced by our previous studies on α_3Y[12,13] as well as the independence of k_{PCET} rate constants on the buffer concentration in the present data. Having shown that 2MP-α_3C is similar to α_3Y in that X_{32} exhibits a low SASA, comparison between the two proteins allows us to investigate the effect of altering the PT driving force. The pK_a value is 1.6 lower for 2MP-α_3C, giving an increase in PT driving force of 95 meV. A change in rate constant by one order of magnitude per pK_a unit is expected for a $PTET_{pre\text{-}eq}$ reaction. Indeed, in the high pH region of Fig. 7, the difference in k_{PCET} between 2MP-α_3C and α_3Y is between one and one and a half orders of magnitude, as expected.

$E^{\circ}(X_{32}^{\bullet}/X_{32}^{-})$ is very similar for 2MP-α_3C (780 ± 4 mV) and α_3Y (749 ± 4 mV). Instead, the lower pK_a value for 2MP-α_3C changes the PT driving force and would mean moving to the right in Fig. 9 for 2MP-α_3C compared to α_3Y. This is consistent with moving from the CEPT region to the $PTET_{pre\text{-}eq}$ region. Indeed, this is what is experimentally observed, as CEPT dominates at low pH for α_3Y, while $PTET_{pre\text{-}eq}$ dominates over almost the entire pH range for 2MP-α_3C with the moderately strong oxidant $[Ru(bpy)_3]^{3+}$ (Fig. 7). When the ET driving force increases by *ca.* 280 meV by using the much stronger oxidant $[Ru(deeb)_3]^{3+}$, we move upwards in the diagram and re-enter the CEPT region, as is shown by the data in Fig. 8. 4MP-α_3C shows an entirely parallel behavior as compared to 2MP-α_3C; the *ca.* 125 mV lower $E^{\circ}(X_{32}^{\bullet}/X_{32}^{-})$ value is not sufficient to favor CEPT with the weaker oxidants, whereas the much greater difference in ΔE° with $[Ru(deeb)_3]^{3+}$ has this effect.

From the more qualitative discussion of changing mechanisms (above), we continue by drawing quantitative comparisons of the rate constants between the different combinations of protein and oxidant with the aid of theories for ET and CEPT. A simplified expression for the free-energy dependence of the rate constant for ET or CEPT is given in eqn (2).[49]

$$k = A \exp\left[\frac{-(\Delta G^{\circ} + \lambda)^2}{4\lambda RT}\right] \quad (2)$$

A CEPT reaction may have contributions to the rate constant from transitions to and from several proton vibrational states that can modify the free-energy prediction of eqn (2). For simplicity these effects will be neglected in the present analysis.[50] The derivative in eqn (3) shows the predicted slope of a typical plot of $\ln k$ *vs.* driving force, where $\partial \ln(k_{CEPT})/\partial(-\Delta G^{\circ}) = (50\ \text{meV})^{-1}$ when $\Delta G^{\circ} = 0$.

$$-\frac{\partial(\ln k)}{\partial(\Delta G^{\circ})} = \frac{1}{2RT}\left(1 + \frac{\Delta G^{\circ}}{\lambda}\right) \quad (3)$$

The driving force for CEPT is given by $\Delta G^{\circ}_{CEPT} = -F(E^{\circ}(Ru^{III}/Ru^{II}) - E^{\circ\prime}(X_{32}^{\bullet}/X_{32}))$ at pH = pK_a of the conjugate acid of the proton acceptor; in these systems water is the proton acceptor, and $pK_a\ (H_3O^+) = 0$. $E^{\circ\prime}(X_{32}^{\bullet}/X_{32})_{pH0}$ can be predicted from the Pourbaix diagrams of α_3Y, 2MP-α_3C, and 4MP-α_3C[5,9] and give $\Delta G^{\circ}_{CEPT} \approx 110$, 55 and −50 meV, respectively, when $[Ru(bpy)_3]^{3+}$ is the oxidant. The PCET reaction is observed even when $\Delta G^{\circ}_{CEPT} > 0$ because the reaction is driven to completion by the more than 100-fold excess of protein *vs.* $[Ru(bpy)_3]^{3+}$ generated per laser flash (*ca.* 1–6 μM), Fig. 4B and E.

As described above, the PCET mechanism is consistent with CEPT when k_{PCET} is pH-independent (at low pH-values, Fig. 7 and 8). The use of $[Ru(deeb)_3]^{3+}$ *in lieu* of $[Ru(bpy)_3]^{3+}$ increases $-\Delta G^{\circ}_{CEPT}$ by 280 meV, and k_{YOH} for 2MP-α_3C and 4MP-α_3C increase by *ca.* two orders of magnitude (Table 4). This corresponds to a slope according to eqn (3) of $(60\ \text{meV})^{-1}$, consistent with CEPT in the normal region with a small driving force.

Shifting the oxidant strength in the CEPT region gives rise to predictable changes in k_{PCET} for each protein individually. Comparing the trend in k_{PCET} between the different proteins, however, does not consistently correlate with changes in ΔG°_{CEPT}. Notably, α_3Y has the least favorable ΔG°_{CEPT}, and yet its CEPT rate constants are the largest (see Fig. 7, low pH region). 4MP-α_3C, which exhibits the most favorable ΔG°_{CEPT} and which is predicted to have its phenol OH consistently in contact with water (Fig. 3, Table S12†), does not have the largest CEPT rate constants, though they are greater than rate constants for 2MP-α_3C. From the study of CEPT in this homogeneous series of proteins, it is clear that factors outside of the driving force influence CEPT rate constants. One possibility is that the vibronic coupling varies significantly among the protein systems due to different proton donor–acceptor distances, which influence the overlap between the proton vibrational wavefunctions. As described above, water is assigned as the dominant primary proton acceptor for the α_3X proteins investigated here. We have previously identified local side chain motions near the Y_{32} site that permit transient access of one to two water molecules to within H-bonding distance of the phenol OH.[13] 2MP-α_3C and 4MP-α_3C behave in a similar manner (Table S12†). The observed differences in the concerted PCET kinetics indicate that α_3Y can access a state or states where the phenol OH and the water proton acceptor are more optimally oriented with respect to PT relative to the MP-α_3C proteins.

At high pH-values, all combinations of protein and oxidant reacted *via* $PTET_{pre\text{-}eq}$. The observed rate constants are proportional to the ET rate constant from deprotonated Y_{32} or MP-C_{32} (k_{YO^-} in eq. (1)), and thus depend on the driving force for ET. The values of k_{YO^-} taken from the fits to eqn (1) in Fig. 7 and 8 are plotted *vs.* the driving force for ET from $Y\text{–}O^-$ to $Ru(L)_3^{3+}$ (Fig. 10). The k_{YO^-} values for MP-α_3C/$[Ru(dmb)_3]^{3+}$ are taken from the rate constants at pH 8.5 and multiplying with $10^{(pK_a - 8.5)}$, *i.e.* assuming that only the second term of eqn (1) is important at pH ≥ 8.5. The data can be fitted with eqn (2), as shown in Fig. 10, with reasonable values of the reorganization energy and pre-exponential factor. k_{YO^-} is a second order rate constant that, below the diffusion-controlled limit, is equal to the product of the equilibrium constant for encounter complex formation with the oxidant (K_d) and the rate constant for unimolecular ET in the encounter complex. It is reasonable to

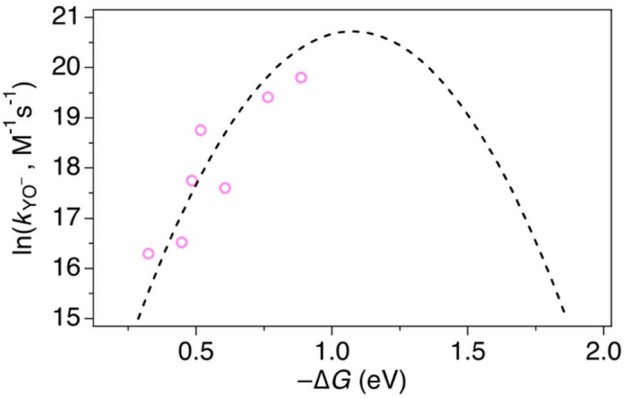

Fig. 10 Natural logarithm (ln) of k_{YO^-} rate constants (pink circles) as a function of driving force for ET from YO^- to the $[Ru(L)_3]^{3+}$ oxidant. The dashed line shows a fit according to eqn (2) assuming $A = 1 \times 10^9$ M^{-1} s^{-1}, which gave $\lambda = 1.1$ eV.

assume that K_d is constant in the present series of reactions, and it is often assumed that $K_d \sim 1$. This means that the second-order rate constant is also expected to follow the free-energy dependence of eq. (2).[49] The good agreement of PTET data and predictions of eqn (2) in Fig. 10 shows that the series of proteins and oxidants form a homogeneous series, where factors that may affect the ET rate constant other than the reaction free energy – such as λ or K_d – remain comparatively constant. Thus, the differences of the PCET rate constants between the proteins discussed in the previous paragraph can be assigned to the PT part of the reaction.

To conclude this section, the free-energy dependencies of both the CEPT and PTET rate constants show that our mechanistic assignments are consistent with current theories. The dependence of the PCET mechanism on oxidant strength and phenolic pK_a can be utilized to analyze and control the mechanism in a rational and predictable way.

Conclusions

2MP-α_3C and 4MP-α_3C were designed with the specific aim of studying the effect of different degrees of solvent exposure on X_{32} properties and PCET reactivity. Both proteins could be oxidized by a series of external $[Ru(L)_3]^{3+}$ complexes with different oxidant strengths ($E^\circ = +1100$–1540 mV *vs.* NHE), and a long-lived neutral radical ($t_{1/2} > 100$ s) was observed. The much greater SASA for the phenol OH of 4MP-α_3C (30–40% *vs.* $\leq \sim 2\%$ for 2MP-α_3C) did not result in any detectable increase in the rate constant for radical formation, however, and did not allow for access of buffer species as primary proton acceptors. A glutamate (E_{13}) was found nearby the phenol O of 2MP-C_{32} in the solution NMR structure (O–O distance 3.2 ± 0.5 Å) and also in QM/MM MD simulations, which led to the expectation of a facilitated PCET by H-bonding and PT to E_{13}. No kinetic evidence for such an effect was detected, and a variant where E_{13} was replaced with alanine (2MP-α_3C-E_{13}A) showed very similar kinetics, with even slightly faster rates. This suggests that the distance and orientation of E_{13} relative to X_{32} are not sufficiently favorable to facilitate proton tunneling, leaving water as the primary proton acceptor for all MP-α_3C proteins.

Instead, we found that the differences in $E^{\circ\prime}$ and pK_a values of 2MP-C_{32}, 4MP-C_{32}, and Y_{32} induced important changes in the rate constants and mechanisms for PCET. With the two weakest $[Ru(L)_3]^{3+}$ oxidants, all three MP-α_3C proteins reacted predominantly by $PTET_{pre\text{-}eq}$ at pH $\gtrsim$ 6, with CEPT being important only at the lowest pH-values examined. This was different from α_3Y, for which CEPT was prominent over a larger pH range and $PTET_{pre\text{-}eq}$ dominated only at pH $\gtrsim$ 8. When the strongest oxidant was used, 2MP-α_3C and 4MP-α_3C showed a similar balance of the two PCET mechanisms as for α_3Y with the weaker oxidant. This can be rationalized by the lower pK_a values for the MP-α_3C proteins, which favor PTET, but with a stronger oxidant the balance is again in favor of CEPT at neutral and acidic pH. Changing $E^{\circ\prime}$ and pK_a values alters ΔG°_{ET} and ΔG°_{PT}, and consequently controls which mechanism dominates the reaction, as is illustrated by the zone diagram reproduced in Fig. 9.

While the difference when changing the oxidant for a given protein can be explained by just changing the driving force (eqn (2)), the difference in k_{CEPT} among the proteins clearly depends also on other factors. Y_{32} has the least favorable ΔG°_{CEPT}, and yet the CEPT rate constant with $[Ru(bpy)_3]^{3+}$ is the largest. Thus, while the three proteins appear to form a homogeneous series when comparing the oxidation rate constants for the deprotonated form (k_{YO^-}), the CEPT reactions differ by more than just their driving forces. MD simulations on the α_3Y and MP-α_3C solution NMR structures revealed fast side chain motions that allow water in and out of the X_{32} site. The observed difference in k_{CEPT} suggests that α_3Y can transiently line up the phenol OH/water H-bond more favorably with respect to PT relative to the two other proteins, giving rise to the somewhat faster k_{CEPT} rate constant.

The present results demonstrate how the PCET mechanism for X_{32} oxidation depends on the driving forces for ET and PT. A sufficiently strong oxidant will favor ETPT and a sufficiently strong base will favor PTET, but if the driving forces for ET and PT are balanced, a concerted CEPT mechanism can dominate. This has implications for enzymes, where the pK_a of residues and reduction potentials can be altered depending on the protein environment. The mechanism in turn determines the rate of the PCET reaction and its dependence on reaction conditions. Our results also show that water is a viable proton acceptor even for amino acids with minimal solvent exposure.

Data availability

Computational data have been deposited in the Open Science Framework Repository (DOI: **https://doi.org/10.17605/OSF.IO/QPFSH**).

Author contributions

R. L. and M. L. generated purified MP-α_3C material for the optical spectroscopy studies. A. N.-M. prepared samples, performed and analyzed all optical spectroscopy measurements. M. L. and C. T. deposited the 4MP-α_3C NMR data and structural

coordinates. C. T. developed the overall MP-α_3C protein design strategy and performed protein structural analyses. C. R. R. performed and analyzed all computational work, under supervision of S. H.-S. P. H. performed and analyzed the EPR experiments. H. A. prepared the oxidant complexes. A. N.-M., S. D. G. S. H.-S., C. T. and L. H. conceived the study, and together with C. R. R. they prepared the manuscript draft and finalized the paper. All authors agreed on the final version of the paper.

Conflicts of interest

There are no conflicts to declare.

Acknowledgements

This work was supported by the Swedish Research Council (grant no. 2020-05246 (L. H.) and grant no. 2017-04992 (S. D. G.)) and the National Institutes of Health grant R01 GM079190 (C. T.). The computational portion of this work was supported by NIH Grant R35 GM139449 (S. H.-S.). C. R. R. was supported by NSF Graduate Research Fellowship Program Grant DGE1752134. Computational resources were provided by the Yale Center of Research Computing. C. R. R. would like to thank Phillips Hutchison for technical assistance. The solution NMR structure of 4MP-α_3C was initially described in the PhD thesis of Dr Melissa C. Martínez-Rivera, University of Pennsylvania, 2013.[18]

References

1 R. Tyburski, T. Liu, S. D. Glover and L. Hammarström, Proton-Coupled Electron Transfer Guidelines, Fair and Square, *J. Am. Chem. Soc.*, 2021, **143**, 560–576.
2 T. Irebo, M. T. Zhang, T. F. Markle, A. M. Scott and L. Hammarström, Spanning four mechanistic regions of intramolecular proton-coupled electron transfer in a Ru(bpy)$_3$(2+)-tyrosine complex, *J. Am. Chem. Soc.*, 2012, **134**, 16247–16254.
3 A. Migliore, N. F. Polizzi, M. J. Therien and D. N. Beratan, Biochemistry and theory of proton-coupled electron transfer, *Chem. Rev.*, 2014, **114**, 3381–3465.
4 S. Hammes-Schiffer and A. A. Stuchebrukhov, Theory of coupled electron and proton transfer reactions, *Chem. Rev.*, 2010, **110**, 6939–6960.
5 C. Tommos, Insights into the Thermodynamics and Kinetics of Amino-Acid Radicals in Proteins, *Annu. Rev. Biophys.*, 2022, **51**, 453–471.
6 C. Tommos, J. J. Skalicky, D. L. Pilloud, A. J. Wand and P. L. Dutton, De novo proteins as models of radical enzymes, *Biochem.*, 1999, **38**, 9495–9507.
7 B. W. Berry, M. C. Martinez-Rivera and C. Tommos, Reversible voltammograms and a Pourbaix diagram for a protein tyrosine radical, *Proc. Natl. Acad. Sci. U. S. A.*, 2012, **109**, 9739–9743.
8 K. R. Ravichandran, A. B. Zong, A. T. Taguchi, D. G. Nocera, J. Stubbe and C. Tommos, Formal reduction potentials of difluorotyrosine and trifluorotyrosine protein residues: Defining the thermodynamics of multistep radical transfer, *J. Am. Chem. Soc.*, 2017, **139**, 2994–3004.
9 S. Hay, K. Westerlund and C. Tommos, Moving a phenol hydroxyl group from the surface to the interior of a protein: effects on the phenol potential and p*K*(A), *Biochem.*, 2005, **44**, 11891–11902.
10 K. R. Ravichandran, L. Liang, J. Stubbe and C. Tommos, Formal reduction potential of 3,5-difluorotyrosine in a structured protein: insight into multistep radical transfer, *Biochem.*, 2013, **52**, 8907–8915.
11 W. Lee, M. Kasanmascheff, M. Huynh, A. Quartararo, C. Costentin, I. Bejenke, D. G. Nocera, M. Bennati, C. Tommos and J. Stubbe, Properties of Site-Specifically Incorporated 3-Aminotyrosine in Proteins To Study Redox-Active Tyrosines: *Escherichia coli* Ribonucleotide Reductase as a Paradigm, *Biochem*, 2018, **57**, 3402–3415.
12 S. D. Glover, C. Jorge, L. Liang, K. G. Valentine, L. Hammarström and C. Tommos, Photochemical tyrosine oxidation in the structurally well-defined alpha3Y protein: proton-coupled electron transfer and a long-lived tyrosine radical, *J. Am. Chem. Soc.*, 2014, **136**, 14039–14051.
13 A. Nilsen-Moe, C. R. Reinhardt, S. D. Glover, L. Liang, S. Hammes-Schiffer, L. Hammarström and C. Tommos, Proton-Coupled Electron Transfer from Tyrosine in the Interior of a *de novo* Protein: Mechanisms and Primary Proton Acceptor, *J. Am. Chem. Soc.*, 2020, **142**, 11550–11559.
14 C. Tommos, K. G. Valentine, M. C. Martinez-Rivera, L. Liang and V. R. Moorman, Reversible phenol oxidation and reduction in the structurally well-defined 2-Mercaptophenol-α_3C protein, *Biochem*, 2013, **52**, 1409–1418.
15 A. Juris, V. Balzani, F. Barigelletti, S. Campagna, P. Belser and A. von Zelewsky, Ru(II) polypyridine complexes: photophysics, photochemistry, electrochemistry, and chemiluminescence, *Coord. Chem. Rev.*, 1988, **84**, 85–277.
16 A. Nilsen-Moe, A. Rosichini, S. D. Glover and L. Hammarström, Concerted and Stepwise Proton-Coupled Electron Transfer for Tryptophan-Derivative Oxidation with Water as the Primary Proton Acceptor: Clarifying a Controversy, *J. Am. Chem. Soc.*, 2022, **144**, 7308–7319.
17 S. D. Glover, R. Tyburski, L. Liang, C. Tommos and L. Hammarström, Pourbaix Diagram, Proton-Coupled Electron Transfer, and Decay Kinetics of a Protein Tryptophan Radical: Comparing the Redox Properties of W32$^{\bullet}$ and Y32$^{\bullet}$ Generated Inside the Structurally Characterized α_3W and α_3Y Proteins, *J. Am. Chem. Soc.*, 2018, **140**, 185–192.
18 M. C. Martínez-Rivera, *Using Model Proteins to Study Tyrosine Oxidation-Reduction: Reversible Voltammograms, Long-Lived Radicals and Detailed Design of the Radical Site*, PhD, University of Pennsylvania, 2013.
19 T. D. Goddard and D. G. Kneller, *SPARKY 3*, University of California, San Francisco, CA, 2008.
20 A. T. Brunger, P. D. Adams, G. M. Clore, W. L. DeLano, P. Gros, R. W. Grosse-Kunstleve, J. S. Jiang, J. Kuszewski, M. Nilges, N. S. Pannu, R. J. Read, L. M. Rice, T. Simonson and G. L. Warren, Crystallography & NMR system: A new software suite for macromolecular structure

determination, *Acta Crystallogr., Sect. D: Biol. Crystallogr.*, 1998, **54**, 905–921.

21 R. Koradi, M. Billeter and K. Wuthrich, MOLMOL: a program for display and analysis of macromolecular structures, *J. Mol. Graph.*, 1996, **14**(51–55), 29–32.

22 M. J. Frisch, G. W. Trucks, H. B. Schlegel, G. E. Scuseria, M. A. Robb, J. R. Cheeseman, G. Scalmani, V. Barone, G. A. Petersson, H. Nakatsuji, X. Li, M. Caricato, A. V. Marenich, J. Bloino, B. G. Janesko, R. Gomperts, B. Mennucci, H. P. Hratchian, J. V. Ortiz, A. F. Izmaylov, J. L. Sonnenberg, D. Williams-Young, F. Ding, F. Lipparini, F. Egidi, J. Goings, B. Peng, A. Petrone, T. Henderson, D. Ranasinghe, V. G. Zakrzewski, J. Gao, N. Rega, G. Zheng, W. Liang, M. Hada, M. Ehara, K. Toyota, R. Fukuda, J. Hasegawa, M. Ishida, T. Nakajima, Y. Honda, O. Kitao, H. Nakai, T. Vreven, K. Throssell, J. J. A. Montgomery, J. E. Peralta, F. Ogliaro, M. J. Bearpark, J. J. Heyd, E. N. Brothers, K. N. Kudin, V. N. Staroverov, T. A. Keith, R. Kobayashi, J. Normand, K. Raghavachari, A. P. Rendell, J. C. Burant, S. S. Iyengar, J. Tomasi, M. Cossi, J. M. Millam, M. Klene, C. Adamo, R. Cammi, J. W. Ochterski, R. L. Martin, K. Morokuma, O. Farkas, J. B. Foresman and D. J. Fox, *Gaussian 16 Revision D.01*, Gaussian, Inc., 2016.

23 C. Lee, W. Yang and R. G. Parr, Development of the Colle-Salvetti correlation-energy formula into a functional of the electron density, *Phys. Rev. B: Condens. Matter Mater. Phys.*, 1988, **37**, 785–789.

24 A. D. Becke, Density-functional thermochemistry. III. The role of exact exchange, *J. Chem. Phys.*, 1993, **98**, 5648–5652.

25 S. Grimme, Semiempirical GGA-type density functional constructed with a long-range dispersion correction, *J. Comput. Chem.*, 2006, **27**, 1787–1799.

26 Y. Zhao and D. G. Truhlar, The M06 suite of density functionals for main group thermochemistry, thermochemical kinetics, noncovalent interactions, excited states, and transition elements: two new functionals and systematic testing of four M06-class functionals and 12 other functionals, *Theor. Chem. Acc.*, 2008, **120**, 215–241.

27 T. H. Dunning Jr, Gaussian basis sets for use in correlated molecular calculations. I. The atoms boron through neon and hydrogen, *J. Chem. Phys.*, 1989, **90**, 1007–1023.

28 D. E. Woon and T. H. Dunning Jr, Gaussian basis sets for use in correlated molecular calculations. III. The atoms aluminum through argon, *J. Chem. Phys.*, 1993, **98**, 1358–1371.

29 Q. Sun, T. C. Berkelbach, N. S. Blunt, G. H. Booth, S. Guo, Z. Li, J. Liu, J. D. McClain, E. R. Sayfutyarova, S. Sharma, S. Wouters and G. K.-L. Chan, PySCF: the Python-based simulations of chemistry framework, *Wiley Interdiscip. Rev.: Comput. Mol. Sci.*, 2018, **8**, 1–15.

30 Q. Sun, J. Yang and G. K.-L. Chan, A general second order complete active space self-consistent-field solver for large-scale systems, *Chem. Phys. Lett.*, 2017, **683**, 291–299.

31 E. R. Sayfutyarova and S. Hammes-Schiffer, Constructing Molecular π-Orbital Active Spaces for Multireference Calculations of Conjugated Systems, *J. Chem. Theory Comput.*, 2019, **15**, 1679–1689.

32 D. A. Case, K. Belfon, I. Y. Ben-Shalom, S. R. Brozell, D. S. Cerutti, I. T. E. Cheatham, V. W. D. Cruzeiro, T. A. Darden, R. E. Duke, G. Giambasu, M. K. Gilson, H. Gohlke, A. W. Goetz, R. Harris, S. Izadi, S. A. Izmailov, K. Kasavajhala, A. Kovalenko, R. Krasny, T. Kurtzman, T. S. Lee, S. LeGrand, P. Li, C. Lin, J. Liu, T. Luchko, R. Luo, V. Man, K. M. Merz, Y. Miao, O. Mikhailovskii, G. Monard, H. Nguyen, A. Onufriev, F. Pan, S. Pantano, R. Qi, D. R. Roe, A. Roitberg, C. Sagui, S. Schott-Verdugo, J. Shen, C. L. Simmerling, N. R. Skrynnikov, J. Smith, J. Swails, R. C. Walker, J. Wang, L. Wilson, R. M. Wolf, X. Wu, Y. Xiong, Y. Xue, D. M. York and P. A. Kollman, *AMBER 2020*, University of California, San Francisco, 2020.

33 J. A. Maier, C. Martinez, K. Kasavajhala, L. Wickstrom, K. E. Hauser and C. Simmerling, ff14SB: Improving the Accuracy of Protein Side Chain and Backbone Parameters from ff99SB, *J. Chem. Theory Comput.*, 2015, **11**, 3696–3713.

34 W. L. Jorgensen, J. Chandrasekhar, J. D. Madura, R. W. Impey and M. L. Klein, Comparison of simple potential functions for simulating liquid water, *J. Chem. Phys.*, 1983, **79**, 926–935.

35 S. D. Glover, G. A. Parada, T. F. Markle, S. Ott and L. Hammarström, Isolating the Effects of the Proton Tunneling Distance on Proton-Coupled Electron Transfer in a Series of Homologous Tyrosine-Base Model Compounds, *J. Am. Chem. Soc.*, 2017, **139**, 2090–2101.

36 W. T. Dixon and D. Murphy, Determination of the acidity constants of some phenol radical cations by means of electron spin resonance, *J. Chem. Soc., Faraday Trans. 2*, 1976, 72.

37 G. Dey, R. Hermann, S. Naumov and O. Brede, Encounter geometry determines product characteristics of electron transfer from 4-hydroxythiophenol to n-butyl chloride radical cations, *Chem. Phys. Lett.*, 1999, **310**, 137–144.

38 C. Tommos, X.-S. Tang, K. Warncke, C. W. Hoganson, S. Styring, J. McCracken, B. A. Diner and G. T. Babcock, Spin-Density Distribution, Conformation, and Hydrogen Bonding of the Redox-Active Tyrosine YZ in Photosystem II from Multiple-Electron Magnetic-Resonance Spectroscopies: Implications for Photosynthetic Oxygen Evolution, *J. Am. Chem. Soc.*, 1995, **117**, 10325–10335.

39 R. S. Mulliken, Electronic Population Analysis on LCAO–MO Molecular Wave Functions. I, *J. Chem. Phys.*, 1955, **23**, 1833–1840.

40 S. Grimme, S. Ehrlich and L. Goerigk, Effect of the damping function in dispersion corrected density functional theory, *J. Comput. Chem.*, 2011, **32**, 1456–1465.

41 W. J. Hehre, R. Ditchfield and J. A. Pople, Self-consistent molecular orbital methods. XII. Further extensions of Gaussian—type basis sets for use in molecular orbital studies of organic molecules, *J. Chem. Phys.*, 1972, **56**, 2257–2261.

42 P. C. Hariharan and J. A. Pople, The influence of polarization functions on molecular orbital hydrogenation energies, *Theor. Chim. Acta*, 1973, **28**, 213–222.

43 T. Clark, J. Chandrasekhar, G. W. Spitznagel and P. V. R. Schleyer, Efficient diffuse function-augmented basis sets for anion calculations. III. The 3-21+G basis set for first-row elements, Li–F, *J. Comput. Chem.*, 1983, **4**, 294–301.

44 M. T. Zhang and L. Hammarström, Proton-coupled electron transfer from tryptophan: a concerted mechanism with water as proton acceptor, *J. Am. Chem. Soc.*, 2011, **133**, 8806–8809.

45 T. Irebo, S. Y. Reece, M. Sjodin, D. G. Nocera and L. Hammarström, Proton-coupled electron transfer of tyrosine oxidation: buffer dependence and parallel mechanisms, *J. Am. Chem. Soc.*, 2007, **129**, 15462–15464.

46 M. Eigen, Proton Transfer, Acid-Base Catalysis, and Enzymatic Hydrolysis. Part I: Elementary Processes, *Angew. Chem.*, 1964, **3**, 1–19.

47 C. Costentin, M. Robert and J.-M. Savéant, Concerted Proton–Electron Transfer Reactions in Water. Are the Driving Force and Rate Constant Depending on pH When Water Acts as Proton Donor or Acceptor?, *J. Am. Chem. Soc.*, 2007, **129**, 5870–5879.

48 R. Tyburski and L. Hammarström, Strategies for switching the mechanism of proton-coupled electron transfer reactions illustrated by mechanistic zone diagrams, *Chem. Sci.*, 2021, **13**, 290–301.

49 R. A. Marcus and N. Sutin, Electron transfers in chemistry and biology, *Biochim. Biophys. Acta, Bioenerg.*, 1985, **811**, 265–322.

50 S. Hammes-Schiffer and A. V. Soudackov, Proton-coupled electron transfer in solution, proteins, and electrochemistry, *J. Phys. Chem. B*, 2008, **112**, 14108–14123.